Resonances in fluid-filled cracks of complex geometry and application to very long period (VLP) seismic signals at Mayotte submarine volcano

Chao Liang [1], Junjun Peng [1], Jean-Paul Ampuero [2], Nathan Shauer [3], Kaoshan Dai [1]

[1]Institute for Disaster Management and Reconstruction (IDMR), Sichuan University, 610207, Chengdu, China

[2]Géoazur, Université Côte d'Azur (UCA), IRD, CNRS, Observatoire de la Côte d'Azur, 06560, Valbonne, France

[3]LabMeC-FECFAU-State University of Campinas, R. Josiah Willard Gibbs 85, Cidade Universitaria, Campinas, 13083-839, SP, Brazil

Key Points:

- Hybrid method combining BEM and FVM efficiently computes resonant frequencies of complex-shaped fluid-filled cracks
- Elliptical crack shares similar modes with rectangular crack but a crack network produces more complex resonances
- A dumbbell-shaped crack explains ratio of first two modes (∼2.5) in the VLP seismic signal at Mayotte submarine volcano

Corresponding author: Chao Liang, chao.liang@scu.edu.cn

Corresponding author: Kaoshan Dai, kdai@scu.edu.cn

Abstract

Fluid-filled cracks sustain a slow guided wave (Krauklis wave or crack wave) whose resonant frequencies are widely used for interpreting long period (LP) and very long period (VLP) seismic signals at active volcanoes. Significant efforts have been made to model this process using analytical developments along an infinite crack or numerical methods on simple crack geometries. In this work, we develop an efficient hybrid numerical method for computing resonant frequencies of complex-shaped fluid-filled cracks and networks of cracks and apply it to explain the ratio of spectral peaks in the VLP signals from the Fani Maoré submarine volcano that formed in Mayotte in 2018. By coupling triangular boundary elements and the finite volume method, we successfully handle complex geometries and achieve computational efficiency by discretizing solely the crack surfaces. The resonant frequencies are directly determined through eigenvalue analysis. After proper verification, we systematically analyze the resonant frequencies of rectangular and elliptical cracks, quantifying the effect of aspect ratio and crack stiffness ratio. We then discuss theoretically the contribution of fluid viscosity and seismic radiation to energy dissipation. Finally, we obtain a crack geometry that successfully explains the characteristic ratio between the first two modes of the VLP seismic signals from the Fani Maoré submarine volcano in Mayotte. Our work not only reveals rich eigenmodes in complex-shaped cracks but also contributes to illuminating the subsurface plumbing system of active volcanoes. The developed model is readily applicable to crack wave resonances in other geological settings, such as glacier hydrology and hydrocarbon reservoirs.

1 Introduction

Slow guided waves that propagate along fluid-filled cracks, named crack waves or Krauklis waves, can be used for inferring the geometries of subsurface cracks and the fluid properties in a wide range of geological settings (Krauklis, 1962; Ferrazzini & Aki, 1987; Paillet & White, 1982; B. Chouet, 1986; Korneev, 2008; Tang & Cheng, 1989; Lipovsky & Dunham, 2015). In volcanology, crack wave resonances along magma-filled sills and dikes have been used for interpreting long period (LP, 0.5-2 s) and very long period (VLP, 2 to 100 s) seismic signals at many volcanos, including Mount Redoubt (B. A. Chouet et al., 1994), Aso (Kawakatsu et al., 2000; Niu & Song, 2020), Galeras (Cruz & Chouet, 1997), Asama (Fujita & Ida, 2003), Kusatsi-Shirane (Kumagai et al., 2003; Nakano & Kumagai, 2005), Etna (Lokmer et al., 2008), and Erebus (Aster, 2019). Crack waves (and

their induced tube waves in wellbores) are used for diagnosing the fracture geometries in unconventional hydrocarbon reservoirs (Henry et al., 2002; Tary et al., 2014; Lipovsky & Dunham, 2015; Liang et al., 2017). The resonating or humming signals in glaciers have also been attributed to crack waves (Métaxian et al., 2003; Stuart et al., 2005; Gräff et al., 2019; McQuillan & Karlstrom, 2021). Natural cracks in the subsurface are complex in shape and usually form an inter-connected network. Therefore, efficient methods for computing resonant modes of single cracks and networks of cracks are necessary for interpreting frequencies measured in the field.

Since its first discovery by Krauklis (1962), crack waves have been studied analytically (Aki et al., 1977; Ferrazzini & Aki, 1987; Korneev, 2008; Lipovsky & Dunham, 2015), experimentally (Tang & Cheng, 1988; Nakagawa et al., 2016; Cao et al., 2021), and numerically by various methods (e.g., B. Chouet, 1986; Yamamoto & Kawakatsu, 2008; Frehner & Schmalholz, 2010; O'Reilly et al., 2017; Liang et al., 2020; Shauer et al., 2021; Jin et al., 2022). Analytically derived dispersion relations are useful for understanding the propagation behavior but are meant for an infinitely long crack and do not account for the restriction of the finite crack tip. The finite difference method (FDM) is normally based on cartesian grids in 2D (Fehler & Aki, 1978) or 3D (B. Chouet, 1986; Liang et al., 2020) and limited to a tabular crack shape. Maeda and Kumagai (2013) and Maeda and Kumagai (2017) performed a large number of numerical simulations on rectangular cracks using a FDM simulator developed by B. Chouet (1986). With that, they obtained a set of empirical fitting formulas for resonant frequencies given the crack aspect ratio α and stiffness ratio $C_L = K_f L/(G w_0)$, where K_f is the fluid bulk modulus, G the solid shear modulus, L the crack length and w_0 the crack aperture. However, such relations only apply to longitudinal or transverse modes on rectangular cracks (Maeda & Kumagai, 2013, 2017). Notably, O'Reilly et al. (2017) simulated a non-planar fluid-filled crack using FDM on a curvilinear grid and adopted a lubrication-type approximation in the fluid (Lipovsky & Dunham, 2015), neglecting fluid acoustics in the crack width direction while resolving the narrow viscous boundary layer close to the crack wall. This treatment removes the time step restriction introduced by extremely fine mesh size in the crack width direction and accelerates the computation. However, their work was limited to 2D geometries. The finite element method (FEM) is more flexible for handling complex crack geometries and has been used to study crack waves in 2D (Frehner & Schmalholz, 2010; Frehner, 2013) and 3D (Shauer et al., 2021). Particularly, Shauer et al. (2021)

produced the first simulation of an elliptical fluid-filled crack using the generalized finite element method (GFEM). However, similar to FDM, FEM needs to discretize the volume, which results in a large number of elements and high computational cost. On the other hand, the boundary element method (BEM) reduces the simulation space from a domain to boundary surfaces, drastically decreasing the number of degrees of freedom, and has been used to study waves in fluid-filled cracks (Yamamoto & Kawakatsu, 2008; Pointer et al., 1998; Jin et al., 2022) and other inclusions (Zheng et al., 2016; Sun et al., 2020). However, previous BEM simulations are either in two dimensions or focus on the wave diffraction instead of analyzing the resonant frequencies. Currently, the study of resonant frequencies of complex-shaped fluid-filled cracks and crack networks in three dimensions remain unknown.

In this work, we propose an efficient hybrid numerical method to simulate crack wave resonance in complex-shaped cracks or crack networks filled with an inviscid fluid, by coupling the boundary element method (BEM) for the solid response and the finite volume method (FVM) for acoustics in the fluid. By using triangular elements in both BEM and FVM on the crack surfaces, we successfully handle complex crack shapes and intersections. We restrict our attention to the low frequency limit where the crack wave is much slower than the solid body waves, such that the solid response can be approximated as quasi-static (Korneev, 2008; Lipovsky & Dunham, 2015; Liang et al., 2020). An eigenvalue analysis is performed to extract the resonant modes directly in the frequency domain, circumventing errors from time discretization and spectral analysis of the time domain simulation data. We first verify our method by comparing results with analytical solutions in the rigid wall limit and with numerical solutions from existing methods for both a rectangular (B. Chouet, 1986; Maeda & Kumagai, 2017) and elliptical cracks (Shauer et al., 2021). An example is then provided to demonstrate the simulation capability for intersecting cracks. The effect of crack aspect ratio and stiffness ratio on resonant frequencies (longitudinal, transverse, and mixed modes) is systematically investigated for both rectangular and elliptical cracks. Although our current model does not include viscous or radiation loss, we provide some theoretical discussion on these effects under simple assumptions (boundary layer limit and quasi-dynamic approximation). Finally, we present a crack shape compatible with the first two spectral peaks of VLP seismic signals from the Fani Maoré, Mayotte submarine volcano and discuss the potential of the methodology for future applications in volcanology and other geological settings.

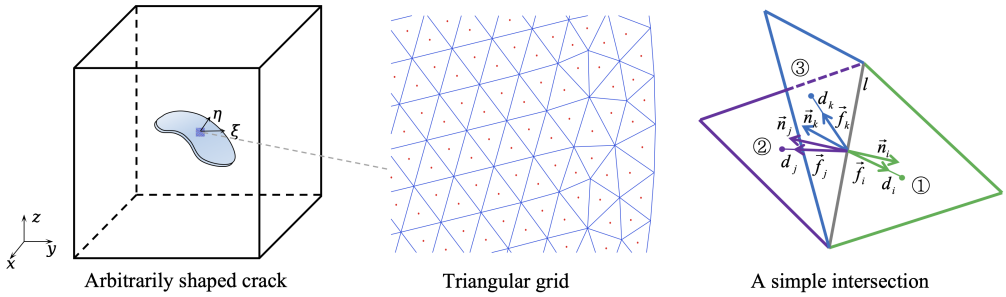

Figure 1. Schematics of an arbitrarily-shaped fluid-filled crack, its spatial discretization (with unknown variables placed in the element centroids, red dots), and a zoom-in view at an intersection between two cracks.

2 Methods

In this section, we present the governing equations, discretization, and eigenmode analysis for computing the resonant frequencies.

2.1 Governing equations

We consider the oscillation of inviscid fluids in complex-shaped thin cracks embedded in a 3D homogeneous linear elastic solid (Figure 1). The initial opening of the crack is w_0, which is assumed to be a constant and much smaller than the wavelength λ. We adopt a similar lubrication approximation as B. Chouet (1986), Yamamoto and Kawakatsu (2008) and O'Reilly et al. (2017), and treat the fluid pressure and velocities as uniform in the crack thickness direction, reducing the crack from a 3D body to a 2D surface S. Following O'Reilly et al. (2017), we consider a small crack curvature so that its effect on the fluid momentum balance is negligible. Thus, the mass and momentum balance of the fluid on the crack surface are written as

$$\frac{1}{w_0}\frac{\partial w}{\partial t} + \frac{1}{K_f}\frac{\partial p}{\partial t} + \frac{\partial v_\xi}{\partial \xi} + \frac{\partial v_\eta}{\partial \eta} = 0, \tag{1}$$

$$\rho_f \frac{\partial v_\xi}{\partial t} + \frac{\partial p}{\partial \xi} = 0, \tag{2}$$

$$\rho_f \frac{\partial v_\eta}{\partial t} + \frac{\partial p}{\partial \eta} = 0, \tag{3}$$

where ρ_f and K_f are fluid density and bulk modulus, w is the crack opening perturbation, p is the fluid pressure perturbation, t is time, and ξ and η are two locally perpen-

dicular coordinates tangent to the crack surface, v_ξ and v_η are the fluid velocities in the ξ and η directions, respectively. Eliminating v_ξ and v_η in (1) using (2)-(3), we have

$$\rho_f \left(\frac{1}{w_0} \frac{\partial^2 w}{\partial t^2} + \frac{1}{K_f} \frac{\partial^2 p}{\partial t^2} \right) - \Delta p = 0, \tag{4}$$

where $\Delta = \frac{\partial^2}{\xi^2} + \frac{\partial^2}{\eta^2}$ is the tangential Laplace operator along the crack surface. The coupling between fluid and solid is encapsulated in the relation between the crack opening perturbation w and pressure perturbation p, which must balance the solid normal stress perturbation σ_n on the crack wall (assumed positive in compression). Since we focus on the low frequency limit, the solid response is approximately quasi-static (Korneev, 2008; Lipovsky & Dunham, 2015; Liang et al., 2020), and p for a linear elastic solid can be expressed as (Segall, 2010):

$$p\left(x\right) = \int_S K\left(x, \xi\right) w\left(\xi\right) dA, \tag{5}$$

where $K(x, \xi)$ is the Green's function that relates a unit open dislocation impulse at ξ to the normal stress change at x. The expressions of K in an elastic whole space and half space are available analytically for a uniform dislocation on both rectangular elements (Okada, 1985, 1992) and triangular elements (Nikkhoo & Walter, 2015).

2.2 Discretization

We discretize the crack surfaces into N_e triangular elements. The unknown average pressures $\bar{\mathbf{p}}$ and openings $\bar{\mathbf{w}}$, placed at element centroids (as shown in Figure 1), are related by

$$\bar{\mathbf{p}} = \mathbf{K}\bar{\mathbf{w}}, \tag{6}$$

where $\mathbf{K}$ is a N_e by N_e matrix and $K(i, j)$ denotes the fluid pressure (or solid normal stress) change at the centroid of the i-th element caused by a unit open dislocation on the j-th element. We use the full space Green's function in this study but one can also use the half space solution.

We then discretize the tangential Laplacian operator by a finite volume scheme with a two-point flux (TPF) approximation following Karimi-Fard et al. (2004), which has been widely used for diffusive flows through a discrete fracture network in hydrocarbon reservoirs (e.g., Li & Lee, 2008; Moinfar et al., 2013; Xu et al., 2017; Berre et al., 2019). This scheme is only first-order accurate and is thus rarely used in wave propagation problems due to the strong numerical diffusion in time domain simulations (e.g., Durran, 2013).

However, it is a sufficient scheme for our problem as we focus on resolving only the spatial distribution of eigenmodes in the frequency domain and the low order of accuracy can be remedied by using more elements. Here, we briefly present the key derivation steps and the readers are referred to Karimi-Fard et al. (2004) for a detailed description.

We consider an arbitrary planar triangular element i with a surface S_i and boundary edges l_{ij}, where j is the index of the neighboring elements. Each i and j pair forms a hydraulic connection. When multiple cracks intersect, multiple connections share the same edge. We integrate equation (4) over each element i's surface, leading to:

$$\rho_f A_i \left[\frac{1}{w_0} \frac{\partial^2 \bar{w}_i}{\partial t^2} + \frac{1}{K_f} \frac{\partial^2 \bar{p}_i}{\partial t^2} \right] = \int_{S_i} \Delta p ds, \tag{7}$$

where

$$\bar{p}_i = \frac{1}{A_i} \int_{S_i} p ds, \tag{8}$$

$$\bar{w}_i = \frac{1}{A_i} \int_{S_i} w ds, \tag{9}$$

are the average pressure and opening of element i, respectively. Applying the divergence theorem to the right hand side of equation (7), we have:

$$\int_{S_i} \Delta p ds = \int_{S_i} \vec{\nabla} \cdot \vec{\nabla} p ds = \int_l \frac{\partial p}{\partial n} dl = -\sum_{j=1}^{n_c} D_{i \to j} Q_{i \to j}, \tag{10}$$

where $\partial p / \partial n$ is the pressure gradient normal to the boundary edges, n_c is the total number of connections in contact with element i, $Q_{i \to j}$ is the flux going out from element i to element j. Since $Q_{i \to j} = -Q_{j \to i}$, we only store $Q_{i \to j}$ for each (i, j) pair and its positive flux direction is pre-defined by an indicator function $I_{i \to j} = -I_{j \to i} = 1$. $D_{i \to j}$ is the discrete divergence operator and $D_{i \to j} = I_{i \to j} = 1$.

The assumption of the TPF scheme is to approximate the flux term in the following form (equation (7) in Karimi-Fard et al. (2004)):

$$Q_{i \to j} = I_{i \to j} T_{ij} (p_i - p_j), \tag{11}$$

where p_i and p_j are pressures defined at the centroids of the two neigboring elements. T_{ij} is the scalar transmissibility and is expressed as

$$T_{ij} = \frac{\alpha_i \alpha_j}{\sum_{k=1}^{n_c} \alpha_k}, \tag{12}$$

$$\alpha_k = \frac{l_{ij}}{d_k} \vec{n}_k \cdot \vec{f}_k, \tag{13}$$

where l_{ij} is the length of the connecting edge, d_k and $\vec{f}_k$ are the length and unit directional vector from midpoint of the edge to the centroid of element k, $\vec{n}_k$ is a unit normal vector perpendicular to the edge and pointing towards element k, as shown in Figure 1. Fluxes on the crack boundaries are set to zero. Combining equations (10) and (11), we have:

$$\int_{S_i} \Delta p ds = -\sum_{j=1}^{n_c} D_{i\to j} I_{i\to j} T_{ij} \left(p_i - p_j\right). \tag{14}$$

It is apparent that changing the positive flux direction from $i \to j$ to $j \to i$ flips the sign of both $D_{i\to j}$ and $I_{i\to j}$ and thus results in the same Laplacian term. Substituting equation (14) into equation (7) and rewriting in the matrix form, we have the spatially discretized equation without external forcing:

$$\rho_f \left(\frac{1}{w_0}\mathbf{K}^{-1} + \frac{1}{K_f}\right) \frac{\partial^2 \bar{\mathbf{p}}}{\partial t^2} = -\mathbf{A}^{-1}\mathbf{D}\mathbf{Q} = -\mathbf{A}^{-1}\mathbf{D}\mathbf{T}\bar{\mathbf{p}}, \tag{15}$$

where $\mathbf{A}$ is a diagonal matrix of size N_e by N_e denoting the area of each element, $\mathbf{Q} = \mathbf{T}\bar{\mathbf{p}}$ is the flux vector whose size is the total number of connections N_c, $\mathbf{T}$ is the transmissibility matrix (including the indicator function) of size N_c by N_e that maps the vector $\bar{\mathbf{p}}$ to $\mathbf{Q}$, and $\mathbf{D}$ is the divergence matrix of size N_e by N_c that maps $\mathbf{Q}$ to the net flux out of each element. The structure of matrices $\mathbf{D}$ and $\mathbf{T}$ for a system of three intersecting crack elements are described in Appendix A.

We further introduce the following dimensionless quantities:

$$\mathbf{K}^* = \mathbf{K}/(G/L), \mathbf{A}^* = \mathbf{A}/L^2, w = w^*/w_0, t^* = t/(L/c_l), \bar{\mathbf{p}}^* = \bar{\mathbf{p}}/(\rho_f c_l^2), \tag{16}$$

where G is the solid shear modulus, L is a representative length of the crack and $c_l = \sqrt{Gw_0/\left(\rho_f L\right)}$ is a representative crack wave speed. Different non-dimensionalization strategies exist, such as the one by B. Chouet (1986) which normalizes wave speeds by the solid compressional wave speed c_p. We choose c_l instead, because in the long wavelength limit, where compliance of the crack dominates, this choice conveniently results in a fundamental frequency of the order of unity. The nondimensionalised equation is

$$\left(\frac{1}{C_L}\mathbf{I} + \left(\mathbf{K}^*\right)^{-1}\right) \frac{\partial^2 \bar{\mathbf{p}}^*}{\partial t^{*2}} = -\mathbf{A}^{*-1}\mathbf{D}\mathbf{T}\bar{\mathbf{p}}^*, \tag{17}$$

where $C_L = K_f L/Gw_0$ is the key dimensionless parameter, named crack stiffness ratio by B. Chouet (1986). The crack wave limit is achieved with $C_L \gg 1$, where the crack is much more compliant than the fluid. C_L can be related to the representative crack wave speed c_l by $C_L = c_f^2/c_l^2$, where c_f is the fluid acoustic wave speed. The crack topol-

ogy (for instance, the aspect ratio α for a rectangular or elliptical crack) and solid Poisson's ratio ν_s are encapsulated into the dimensionless stiffness matrix $\mathbf{K}^*$. The solid Poisson's ratio is set to 0.25 throughout this manuscript, unless otherwise mentioned.

2.3 Eigenmode analysis

We directly obtain the resonant frequencies through eigenmode analysis in the frequency domain. The spatially discretized dimensionless equation is written as

$$\frac{\partial^2 \bar{\mathbf{p}}^*}{\partial {t^*}^2} = -\mathbf{B}\bar{\mathbf{p}}^*, \tag{18}$$

where

$$\mathbf{B} = \left(\frac{1}{C_L}\mathbf{I} + (\mathbf{K}^*)^{-1}\right)^{-1} {\mathbf{A}^*}^{-1}\mathbf{D}\mathbf{T}. \tag{19}$$

The nondimensionalised Fourier transform is defined as

$$\hat{u}\left(\omega^*\right) = \int_{-\infty}^{+\infty} u\left(t^*\right) e^{i\omega^* t^*} dt^*, \tag{20}$$

where

$$\omega^* = \omega / \left(c_l / L\right), \tag{21}$$

is the dimensionless angular frequency. The dimensionless frequency is

$$f^* = \omega^*/(2\pi) = f/(c_l/L). \tag{22}$$

Taking the Fourier transform of equation (18), we have:

$$\left(\omega^*\right)^2 \hat{\bar{\mathbf{p}}} = \mathbf{B}\hat{\bar{\mathbf{p}}}, \tag{23}$$

where $\left(\omega^*\right)^2$ and $\hat{\bar{p}}$ are the eigenvalues and eigenvectors of the real matrix $\mathbf{B}$. Since we deal with inviscid fluids, we only seek real positive eigenvalues, which correspond to undamped oscillatory modes. The resulting eigenvectors determine the spatial distribution of the pressure on the crack surface. Solving the resonant frequencies in dimensionless form is advantageous, because one can easily scale the solution to other parameters, such as crack length, crack width and solid stiffness, given the same dimensionless parameters, C_L, ν_s and crack topology.

3 Verification and examples

In this section, we first verify our implementation by comparing our results to analytical solutions in the rigid solid limit and numerical solutions from existing studies.

We then present an example of simple intersecting crack geometry to demonstrate the utility of our method.

Table 1. The error between the theoretical and numerical resonant frequencies for the first 16 modes

Mode	Theoretical value	Numerical value	Error (%)
1	0.5000	0.5004	0.074
2	0.8333	0.8325	0.105
3	0.9718	0.9706	0.127
4	1.0000	1.0008	0.078
5	1.3017	1.3018	0.009
6	1.5000	1.5010	0.066
7	1.6667	1.6647	0.118
8	1.7159	1.7172	0.072
9	1.7401	1.7370	0.175
10	1.9437	1.9413	0.122
11	2.0000	2.0014	0.068
12	2.1667	2.1693	0.123
13	2.2423	2.2409	0.060
14	2.5000	2.4954	0.184
15	2.5000	2.5010	0.042
16	2.5495	2.5426	0.270

3.1 Comparison with analytical solutions in a rigid solid

We compute the **K** matrix using the subroutines developed by Nikkhoo and Walter (2015), which have been extensively used by other studies. The bulk part that needs to be validated is the FVM discretization of the Laplacian term. For that, we set solid rigidity to infinity and compare the numerical results to the analytical solution of the resonant frequencies of linear acoustic waves in a 2D rectangular domain with zero-flux boundaries (Rona, 2007). The solution is in a dimensionless form with a rectangular domain of size 1 by 0.5 and a wave speed of 1. The comparison results for the first 16 modes are tabulated in Table 1. The excellent agreement between our numerical results and the

analytical solutions, with relative differences smaller than 0.2%, verifies our FVM discretization of the Laplacian term.

3.2 Comparison to numerical solutions by existing studies

We compare solutions by our method (BEM+FVM) to those by B. Chouet (1986), Maeda and Kumagai (2017) and Shauer et al. (2021). With B. Chouet (1986) and Maeda and Kumagai (2017), we compare resonant frequencies of longitudinal modes for a rectangular crack for various values of C_L (5, 15, 25, 50, 75, 100). With the GFEM by Shauer et al. (2021), we compare solutions of multiple modes on both rectangular and elliptical cracks. The eigenmodes can be straightforwardly classified as longitudinal (variation only along the major crack axis), transverse (variation only along the minor crack axis), and mixed modes for a rectangular crack, but less so for an elliptical crack. Since the method by Shauer et al. (2021) discretizes the problem in time and, therefore, does not readily provide resonant frequencies, we ran their code to excite the fluid oscillation on the crack with $C_L = 100$ by a point injection source and then extract the resonant frequencies from the spectral peaks of the pressure records at a few receiving points. We use a Gaussian time function for the injection source $f(t) = \exp\left(-(t-t_c)^2/T^2\right)$ with $t_c = 0.5$, $T = 0.1$, to ensure a smooth start and a sufficiently wide spectrum to cover enough eigenmodes. Note that if either excitation or receiving points are placed on the nodal line, the eigenmode can not be excited or recorded. Therefore, not all eigenmodes are excited in the time domain simulation and we also only compare selective modes with Shauer et al. (2021), which is sufficient for verification purposes. The detailed geometries and simulation data are presented in Appendix B. Notably, the code of Shauer et al. (2021) has the capability of both considering (fully dynamic, FD) or neglecting the solid inertia (quasi-static, QS), allowing to investigate the impact of the solid inertia on crack wave resonant frequencies.

Tables 2 and 3 show the comparison of dimensionless resonant frequencies of seletive eigenmodes from the GFEM program by Shauer et al. (2021) with those by our method for a rectangular and elliptical crack, respectively, with an aspect ratio of 0.5, major axis length of 1, and C_L of 100. The relative difference between our results and those from Shauer et al. (2021) are near 2% or less, with or without solid inertia. This close agreement not only demonstrates the validity of our approach but also reassures that the quasi-static solid response is a very good approximation when computing the

Table 2. Resonant frequencies by BEM+FVM and GFEM with or without inertia (FD or QS), rectangular crack

Mode	Resonant frequencies detected at receiving points by GFEM						BEM+FVM	Error FD (%)	Error QS (%)
	(-0.5, 0)		(-0.2, 0.25)		(0, 0.25)				
	FD	QS	FD	QS	FD	QS			
1	**1.236**	**1.236**	1.236	1.236			1.210	2.15	2.15
2	**2.727**	**2.691**					2.662	2.44	1.09
3			**2.890**	**2.873**	2.818	2.782	2.835	1.94	1.34
4			**3.453**	**3.418**			3.373	2.37	1.33
5	**4.454**	**4.400**	4.436	4.382			4.385	1.57	0.34
6					**4.526**	**4.491**	4.466	1.34	0.56
7			**6.035**	**5.964**			5.980	0.92	0.27
8	**6.399**	**6.273**			6.344	6.236	6.330	1.09	0.90

The bold values are used for error calculation. We use a of CL=100 and aspect ratio of 0.5

Mode eigenfunctions are shown in Figure 2.

Table 3. Resonant frequencies by BEM+FVM and GFEM without inertia (QS), elliptical crack

Mode	The resonant frequencies can be detected at detection points			BEM+FVM	Error (%)
	(-0.5, 0)	(0, 0.25)	(0, 0)		
1	**1.527**			1.518	0.59
2	**3.027**		3.090	3.050	0.75
3		**3.290**		3.241	1.51
5	**4.890**			4.816	1.54
7	**6.890**	6.853	6.944	6.771	1.76
8		7.308	**7.235**	7.107	1.80

The bold values are used for error calculation. We use a of CL=100 and aspect ratio of 0.5

Mode eigenfunctions are shown in Figure 3.

crack wave resonant frequencies, at least for a C_L of 100. A similar conclusion has also been reached by Shauer et al. (2021). Since we assume a quasi-static solid response, it is reasonable that our results have a better agreement to those by GFEM without inertia.

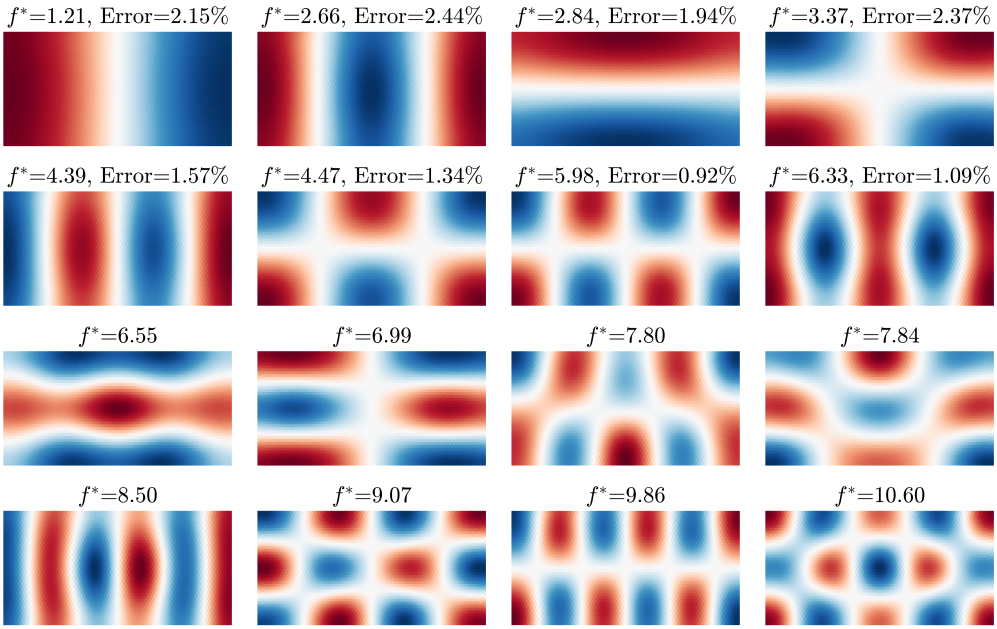

Figure 2. Dimensionless frequencies and eigenfunctions of the first 16 resonant modes (numbered in an ascending order in frequencies) of a rectangular crack with C_L=100 and aspect ratio of 0.5 calculated by BEM+FVM. The errors of selective resonant frequencies between the BEM+FVM and GFEM without inertia are shown in Table 2. The white color indicates the nodal lines.

The pressure eigenfunctions of the first 16 resonant modes are displayed in Figure 2 for a rectangular crack and Figure 3 for an elliptical crack, showing a rich spectrum of spatial variations including longitudinal, transverse, and mixed modes. Different modes can produce different near and far field radiation patterns, that may be detectable in real seismic data (e.g., Liang et al., 2020).

The dimensionless frequencies of the first 9 longitudinal modes for rectangular cracks by various methods with different crack stiffness ratios are shown in Figure 4. The results of Shauer et al. (2021) are only computed for a C_L of 100. For ease of comparison, we convert dimensionless frequencies f^* in our studies to those in B. Chouet (1986) ${f_C}^*$,

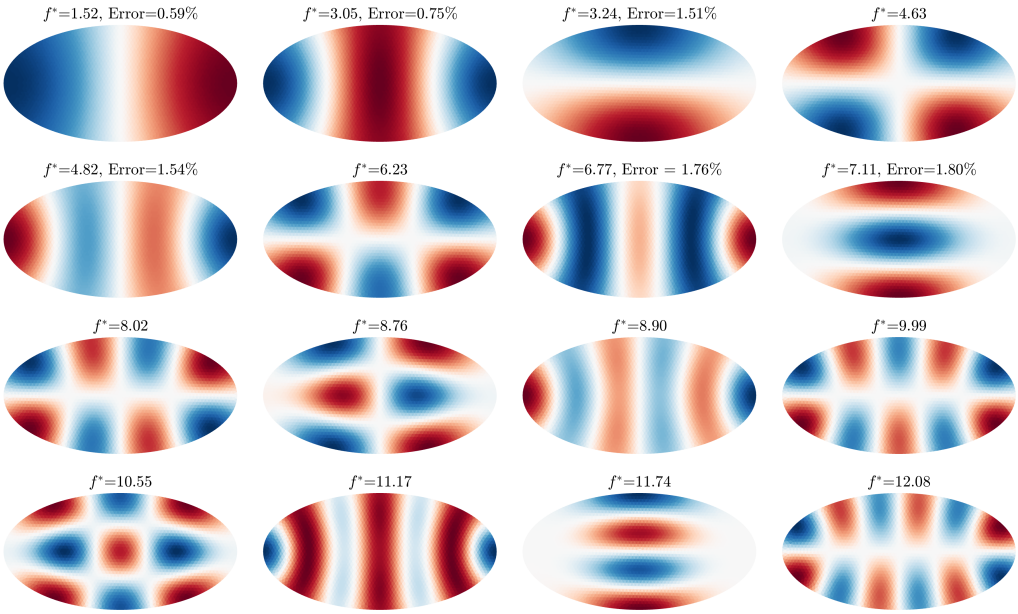

Figure 3. Same as Figure 2 but for an elliptical crack.

which are related by $f_C^* = f^* c_l / c_P$. Overall, our results match well with those by Shauer et al. (2021) (relative error $< 3\%$) and also qualitatively well with those by B. Chouet (1986) and Maeda and Kumagai (2017). However, there are quantitative discrepancies between our results and those by B. Chouet (1986) (relative error 8.83-23.43%) and Maeda and Kumagai (2017) (relative error 2.72-16.63%, see the supporting information for tabulated errors). Particularly, both B. Chouet (1986) and Maeda and Kumagai (2017) systematically give lower frequencies than those by our method and Shauer et al. (2021). We suspect these discrepancies are likely due to differences in spatial and temporal sampling, or domain sizes used in the FDM code in B. Chouet (1986) and Maeda and Kumagai (2017). Particularly, a truncated domain in the FDM results in a more compliant solid response (Korneev et al., 2014), which in turn results in a lower crack wave speed and resonant frequencies. Our method uses boundary elements and thus an infinite domain is directly satisfied. For this reason, when comparing results with Shauer et al. (2021), we deliberately used a very large domain (10 times the length of the crack) in the GFEM code to minimize its boundary effect using an unstructured grid, coarsening in regions far from the crack.

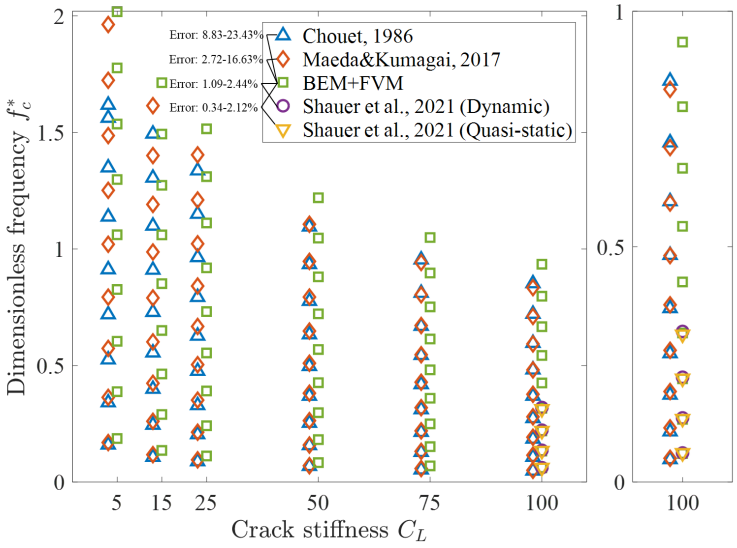

Figure 4. Dimensionless frequencies f_C^* of longitudinal modes for rectangular cracks with different C_L (5, 15, 25, 50, 75, 100) by various methods, and a zoom-in view of the case $C_L = 100$ on the right panel. Results by B. Chouet (1986) and Maeda and Kumagai (2017) are slightly shifted in the horizontal axis to avoid overcrowding the figure.

3.3 An example of intersecting cracks

We now apply our method to one example of intersecting cracks, one full ellipse with a half-elliptical branch, and obtain the first 16 eigenmodes, shown in Figure 5. Interactions between multiple cracks result in more complex resonant modes than in single cracks (shown in Figures 3 and 4). For example, the fundamental mode now involves fluid exchange between the major crack and the branch, and has a lower frequency than the fundamental mode of the major crack (the second mode in this case). When nodal lines coincide with the intersecting edge, resonances can be isolated on the major crack, such as modes 2, 7, 8, 13 and 16. Temporal manifestation of these modes requires a more peculiar condition: the excitation must not be located in the branch. One can certainly add more complexities in the crack network, such as asymmetries, non-planarity or more intricate coupling, and expect to encounter richer eigenmodes. However, such modeling only becomes meaningful when more compelling observations exist and require. We will demonstrate later how a particular crack shape can explain the ratio of the first two spectral peaks in the VLP seismic data at the Fani Maoré, Mayotte submarine volcano. Ex-

cept for that, we decide to leave the analysis of eigenmodes of a more complex crack network for future investigation.

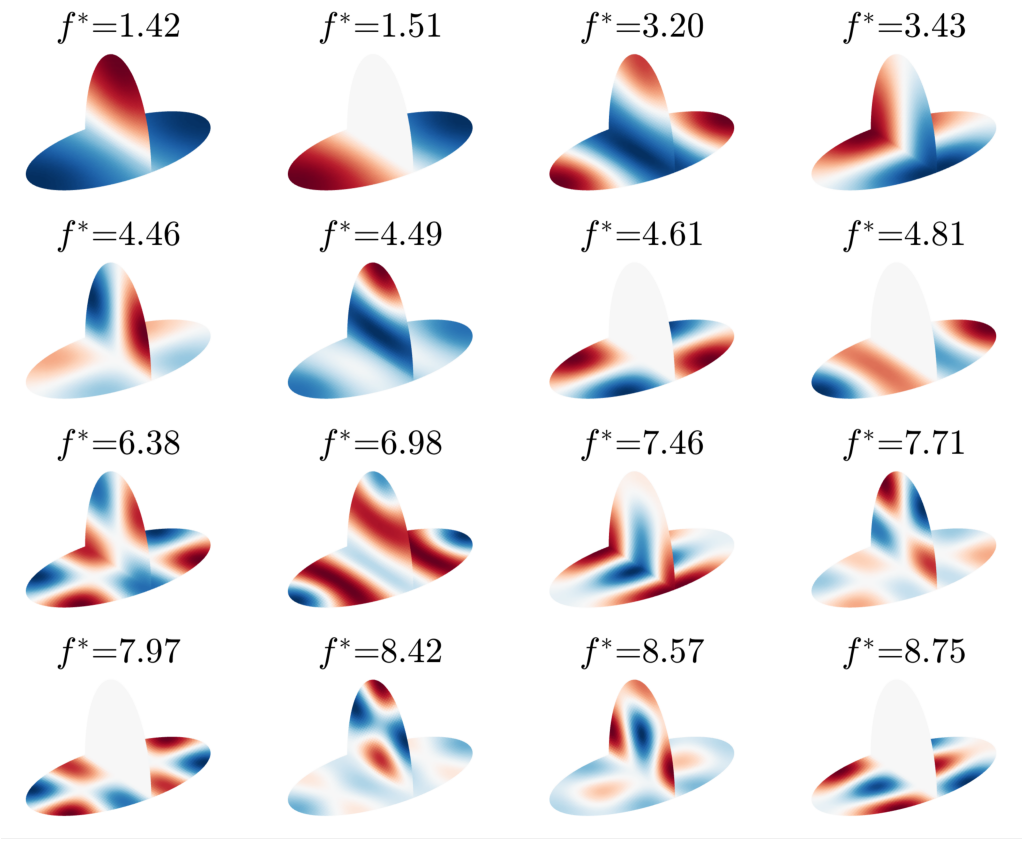

Figure 5. The first 16 eigenmodes of a simple two-intersecting-cracks geometry: a half ellipse intersecting a full ellipse (aspect ratio 0.5) along its minor axis. The major axis length of the full elliptical crack is chosen as L for the non-dimensionalisation.

4 Effect of aspect ratio α and crack stiffness ratio C_L

In this section, we present the effect of α and C_L on the resonant frequencies of rectangular and elliptical cracks, with major and minor axes in the $x-$ and $y-$directions, respectively. Maeda and Kumagai (2017) presented a similar analysis for rectangular cracks, but only on longitudinal and transverse modes. Here, we include the mixed modes and the results for elliptical cracks. We fixed $C_L = 100$ when varying α (from 0.05 to 1.00 with an increment of 0.05) and fix $\alpha = 0.5$ when varying C_L (from 5 to 100 with an increment of 5). The frequencies of the first 16 eigenmodes are tabulated in the Support-

ing information. Here, we select 9 representative modes and visualize them in Figures 6-9. For rectangular cracks, we associate to each mode a pair of numbers (i, j) that denote the number of half wavelengths in the $x-$ and $y-$directions. For instance, the fundamental mode $(1, 0)$ is a longitudinal mode with one half wavelength pressure variation in the $x-$direction and quasi-uniform in the $y-$direction. Such numbering becomes less obvious for elliptical cracks, especially when the aspect ratio approaches 1, for which the eigenfunctions are better characterized by radial and circumferential variations. Nonetheless, for the ease of comparing results with rectangular cracks, we still number the representative modes in Figures 7 and 9 approximately into longitudinal, transverse, and mixed modes.

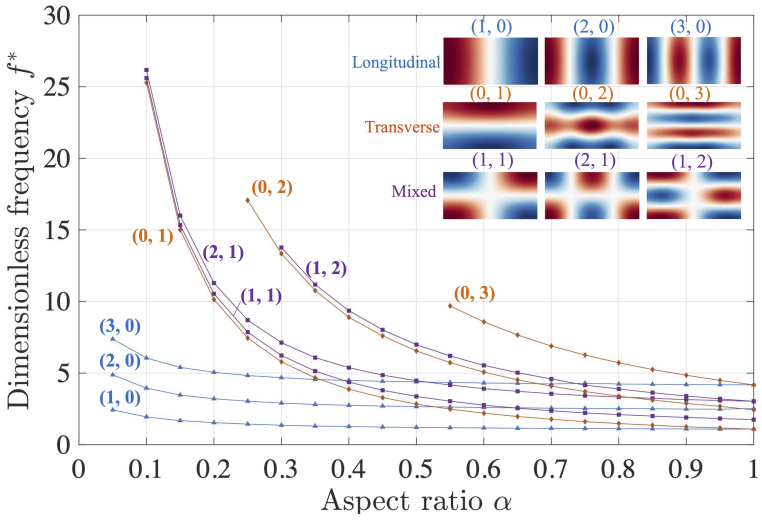

Figure 6. Dimensionless resonant frequencies of representative modes of rectangular cracks as a function of the aspect ratio α. C_L is fixed to 100. The eigenfunctions displayed are for an aspect ratio of 0.55. Certain high order mixed and transverse modes rank outside of the first 16 eigenmodes that we store, which causes the apparent absence of data at low aspect ratios.

4.1 Effect of aspect ratio

The variation of resonant frequencies with aspect ratio is shown in Figure 6 and 7 for rectangular and elliptical cracks, respectively. For both cases, decreasing the aspect ratio increases the crack stiffness from the transverse direction and results in higher resonant frequencies for all the modes. This effect is relatively mild for longitudinal modes but rather steep for transverse and mixed modes. For instance, when α of a rectangu-

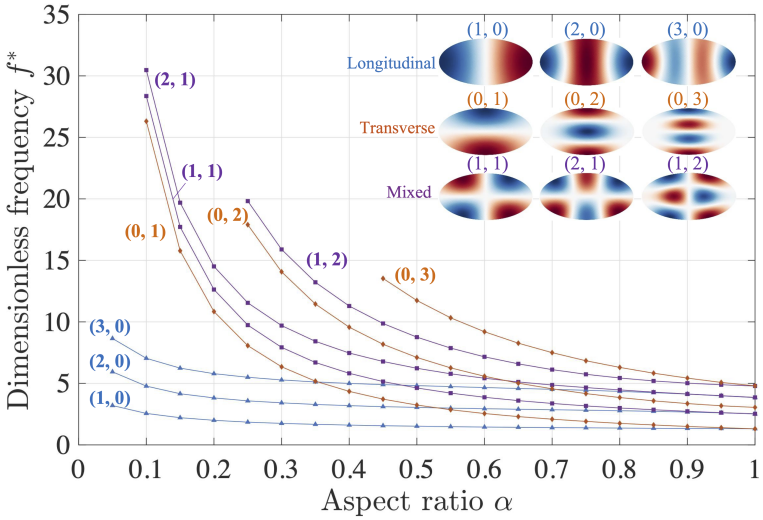

Figure 7. Same as Figure 6 but for elliptical cracks. Note that the mode numbers (i, j) are not strictly valid for an elliptical crack but are useful for our interpretation (more explanation in the main text).

lar crack decreases from 1.0 to 0.1, the frequency of the fundamental mode $(1, 0)$ increases by ~ 1.8 fold while the frequency of the mixed mode $(1, 1)$ increases by ~ 14.6 fold. As a result, the first few resonant modes are predominantly longitudinal for both rectangular and elliptical cracks at low aspect ratios (below 0.2). For a similar mode, the resonant frequency of an elliptical crack is consistently higher than that of the rectangular crack. This is expected as the elliptical crack is narrower in the transverse direction and thus stiffer than a rectangular crack of the same length and aspect ratio.

Another clear feature, for both rectangular and elliptical cracks, is that frequencies of modes with same wavelengths in the transverse direction converge as α decreases. For instance, frequencies of mixed modes (1, 1) and (2, 1) converge to the values of transverse mode (0, 1). Similar convergence also exists for modes (0, 2) and (1, 2). This is expected because the crack wave speed, in the limit of low aspect ratio, is primarily controlled by the short wavelength in the transverse direction. As α increases, the frequencies of different modes become more intermingled and mode degeneration occurs, where modes with distinct eigenfunctions share the same frequency. It is well known that mode degeneration occurs at $\alpha = 1$ due to the geometric symmetry of a square or circle. What we show here is that mode degeneration also occurs at intermediate aspect ratios. For

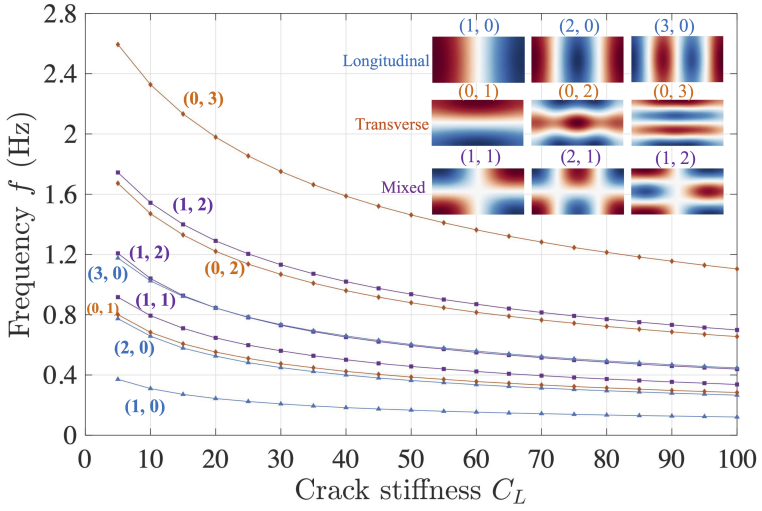

Figure 8. Resonant frequencies of representative modes of rectangular cracks as a function of the crack stiffness C_L. The aspect ratio α is set as 0.5

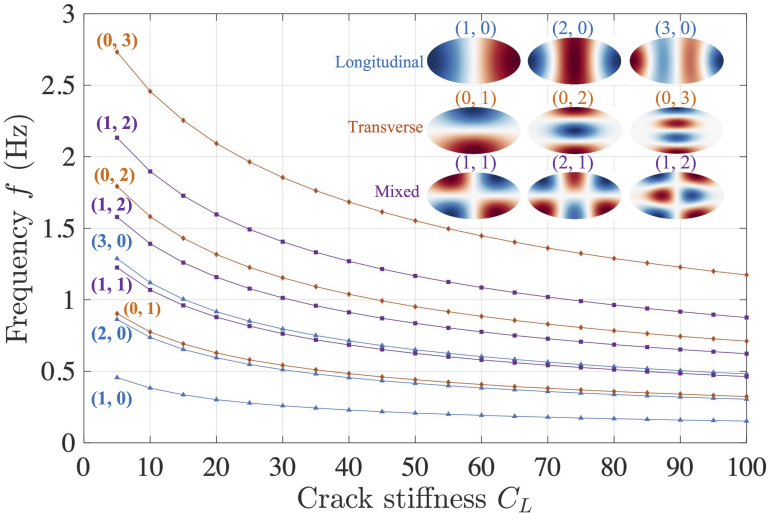

Figure 9. Same as Figure 8 but for elliptical cracks

instance, modes (3, 0) and (0, 1) for both a rectangular and elliptical crack share similar frequencies when $\alpha \approx 0.35$.

4.2 Effect of crack stiffness ratio

Since the normalization constant $(c_f/\sqrt{C_L})/L$ for frequency changes with C_L, we visualize the actual resonant frequency f, instead of f^*. We use $c_f = 1$ m/s and $L = 1$ m to scale f^* to f. C_L is the key dimensionless parameter that controls the crack wave

propagation: the higher the value of C_L, the lower the phase velocity (e.g., B. Chouet, 1986; Maeda & Kumagai, 2017). As a result, the resonant frequencies of all modes for both rectangular (Figure 8) and elliptical cracks (Figure 9) decrease continuously as C_L increases. Again, for a similar mode, the resonant frequencies of an elliptical crack is consistently higher than those of a rectangular crack given the same axial lengths.

5 Energy dissipation

Since we currently focus on computing crack resonant frequencies in complex crack geometries, we assume both an inviscid fluid and a quasi-static solid and we do not consider energy dissipation, from either fluid viscosity or seismic radiation. When damping exists, the resonant frequency becomes complex and the rate of decay is quantified by the quality factor

$$Q = \frac{\mathrm{Re}\,(f)}{2\mathrm{Im}\,(f)}, \tag{24}$$

which is also the number of cycles for an oscillation's energy to fall off to $e^{-2\pi} \sim 0.2\%$ of its original value. The effect of viscous damping has been investigated analytically with fully dynamic (Korneev, 2008) and quasi-static solid response (Lipovsky & Dunham, 2015) on an infinite crack. However, the applicability of the Q formula on a finite crack has not yet been tested. In addition, the convoluted derivation in Korneev (2008) makes it difficult to quantify the relative contribution of different dissipative sources to the total energy loss. On the other hand, numerical studies on rectangular cracks (e.g., Kumagai & Chouet, 2000) have investigated the Q caused by seismic radiation but adopted a simplistic treatment of the fluid viscosity, either an inviscid or fully-developed flow. In this section, we offer a semi-analytical discussion of energy dissipation under a few assumptions and attempt to address two questions: (1) does the formula of Q developed by Lipovsky and Dunham (2015) for an infinite crack also apply to a finite crack? (2) which of the two sources of energy dissipation, fluid viscosity and seismic radiation, is more significant?

5.1 The applicability of Q formula from dispersion to a finite crack

We consider a viscous fluid with kinematic viscosity μ. To focus on the effect of the finite geometry, we compare analytical solutions by Lipovsky and Dunham (2015) to numerical solutions by Liang et al. (2020) for a rectangular crack, both of which as-

sume a quasi-static solid response. For simplicity, we focus on the boundary layer limit

$$\zeta = w_0/\sqrt{4\nu/\omega} \gg 1, \tag{25}$$

where the crack aperture w_0 is much larger than the thickness of the viscous boundary layer $\sqrt{4\upsilon/\omega}$. In this limit, Q is high and ω can be well approximately by the inviscid solution. The analytical formula of Q for crack waves with real wavenumber is given by equation (80) in Lipovsky and Dunham (2015) and, after neglecting the small imaginary part of phase velocity when $\zeta \gg 1$, we have:

$$Q = \sqrt{2}\zeta. \tag{26}$$

The hypothesis is that this expression for Q also holds, at least approximately for a finite rectangular crack, regardless of its geometric shape, as long as w_0, μ and ω are known. We perform numerical simulations using the program by Liang et al. (2020), who employed a finite difference method on a stretched grid to deal with the narrow viscous boundary layer. We set $L = 100$ m, $K_f = 1$ Pa, $G = 1$ Pa, $w_0 = 1$ m, which results in a C_L of 100, and solve for the inviscid resonant angular frequencies ω of rectangular cracks of two aspect ratios, 0.5 and 1.0. We then adjust μ so that ζ takes the values of 10, 20, 40, 60, 80, 100 and 200. We consider the first two modes of the crack with aspect ratio of 0.5 and the fundamental mode of the square crack to represent different mode types and crack shapes. The Q values of viscous cases are obtained using the methodology by Liang et al. (2020) and the comparison to equation (26) is shown in Figure 10.

As shown in Figure 10, the prediction by the analytical formula in Lipovsky and Dunham (2015) matches well the numerical solutions. The agreement gets better at large ζ, where the assumption of boundary layer limit becomes more accurate. The differences between the numerical and analytical solutions are less than 5% at $Q > 40$, while the difference at $Q = 10$ is $\sim 14\%$. Another encouraging finding is that aspect ratios and mode numbers of rectangular cracks have a negligible impact on the value of Q as long as ζ is the same. We thus postulate that the Q formula is likely to hold also for other crack shapes or even a crack network. We further propose that one may first approximate the resonant frequency ω of complex shaped cracks using the inviscid solution efficiently determined by our method, and then directly estimate Q using the analytical formula. However, future numerical studies considering both complex crack geometry and fluid viscosity are necessary to rigorously test this hypothesis.

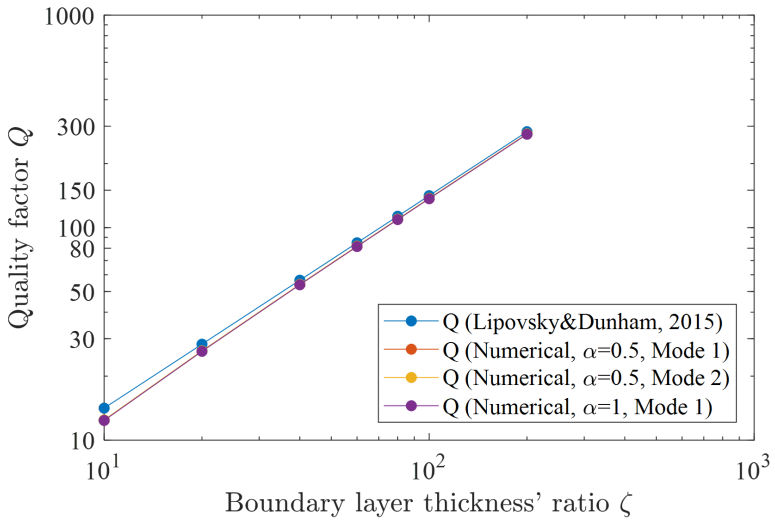

Figure 10. Quality factor of various resonant modes of rectangular cracks as a function of the boundary layer thickness ratio ζ.

5.2 The competition between radiation and viscous damping

Instead of considering the fully dynamic solid response (e.g., Korneev, 2008), we assume a quasi-dynamic solid response (e.g., Rice, 1993; Geubelle & Rice, 1995), which allows to explicit extract the instantaneous long wavelength emission perpendicular to the crack surface, the radiation damping (RD) term. We also consider an infinite crack in two dimensions for the ease of theoretical treatment following Lipovsky and Dunham (2015). By neglecting the wave mediated stresses and the seismic diffraction at the finite crack tips, the radiation we consider is an underestimate, but it is still useful for understanding the relative importance of various dissipation sources. Since resonances tend to be overdamped in the fully developed flow limit $\zeta \gg 40$ (Korneev, 2008; Lipovsky & Dunham, 2015), we continue to focus on the boundary layer limit $\zeta \ll 40$. We explicitly identify the radiation and viscous damping terms in the governing equation and then compute the ratio of their magnitudes.

The width-averaged crack wave equation considering viscous wall traction is obtained by combining the mass and momentum balance equations in Lipovsky and Dunham (2015),

$$\frac{\rho_f}{K_f}\frac{\partial^2 p}{\partial t^2} + \frac{\rho_f}{w_0}\frac{\partial^2 w}{\partial t^2} - \frac{\partial^2 p}{\partial x^2} - \frac{2}{w_0}\frac{\partial \tau}{\partial x} = 0, \tag{27}$$

where τ is the wall shear traction. We introduce the double Fourier transform of an arbitrary function $F(x,t)$ as

$$\hat{F}(k,\omega) = \int_{-\infty}^{+\infty}\int_{-\infty}^{+\infty} F(x,t)\, e^{-i(kx-\omega t)} dt dx. \tag{28}$$

Applying it to equation (27) leading to

$$-\omega^2 \rho_f \left(\frac{\hat{p}}{K_f} + \frac{\hat{w}}{w_0}\right) + k^2 \hat{p} - ik\frac{2}{w_0}\hat{\tau} = 0. \tag{29}$$

Using equation (38) in Lipovsky and Dunham (2015) and neglecting horizontal wall motion, the wall shear traction is related to fluid pressure by

$$\hat{\tau} = -ikw_0 \Omega \hat{p}/2, \tag{30}$$

where

$$\Omega = \left(\sqrt{i}/\zeta\right) \tanh\left(\zeta/\sqrt{i}\right), \tag{31}$$

and tends to $\sqrt{i}/\zeta$ in the boundary layer limit. Therefore, the viscous damping (VD) term in the equation is

$$VD = k^2 \Omega \hat{p}. \tag{32}$$

Applying the quasi-dynamic solid response (Geubelle & Rice, 1995), the fluid pressure and crack opening are related by

$$\hat{p} = \frac{Gk\hat{w}}{2(1-\upsilon_s)} - i\omega\eta_R \hat{w}, \tag{33}$$

where the two terms on the right hand side are the quasi-static response and radiation damping (RD), respectively, and $\eta_R = \rho_s c_p/2$ is the radiation damping coefficient. The ratio between the QS and RD terms is approximately $c_s^2/(c_p c)$ (dropping terms involving Poisson's ratio), where $c = \omega/k$ is the crack wave phase velocity. In the low-frequency limit, which we are interested in, the crack wave speed is much smaller than the speeds of the solid body waves, $c \ll c_s \sim c_p$, and thus the RD term is much smaller than the QS term. Substituting equation (33) into (29) and approximating $\hat{w}/\hat{p}$ using the QS part, we obtain the RD term in equation (29) as

$$RD = i\omega^3 \frac{\rho_f n_R}{K_f}\hat{w} \approx i\omega^3 \frac{\rho_f n_R}{K_f}\frac{2(1-\upsilon_s)}{Gk}\hat{p}. \tag{34}$$

The ratio between RD and VD is

$$\frac{RD}{VD} = ic^3 \frac{\rho_f n_R}{K_f}\frac{2(1-\upsilon_s)}{G\Omega} = i\frac{c_p c^3}{c_f^2 c_s^2}\frac{(1-\upsilon_s)}{\Omega}. \tag{35}$$

In the boundary layer limit, the magnitude of this ratio becomes

$$\left|\frac{RD}{VD}\right| = \frac{c_p c^3}{c_f^2 c_s^2}\zeta\left(1-\upsilon_s\right). \tag{36}$$

When the overall damping is small, the crack wave phase velocity as a function of wavelength λ is well approximated by the inviscid dispersion relation:

$$c = \sqrt{\frac{2\pi G w_0}{\lambda\rho_f\left(1-\upsilon_s\right)}} \sim c_f/sqrtC_\lambda, \tag{37}$$

where $C_\lambda = K_f\lambda/Gw_0$ is a crack stiffness ratio similar to C_L but replacing L by λ. Finally, we obtain RD/VD, which scales as

$$\left|\frac{RD}{VD}\right| \sim \frac{c_p c_f}{c_s^2}\frac{\zeta}{C_\lambda^{3/2}} = \frac{c_p c_s}{c_f^2}\zeta\left(\frac{w_0\rho_s}{\lambda\rho_f}\right)^{3/2}, \tag{38}$$

after dropping small constants such as 2, π and μ_s. $|RD/VD|$ is governed by three dimensionless parameters: $\frac{c_p c_f}{c_s^2}$, C_λ and ζ. The first parameter one is controlled by the body wave speeds of the solid and fluid and is not related to the crack geometry. For a typical crustal rock and liquid fluid, for instance with $c_f = 1500$ m/s, $c_p = 4500$ m/s, and $c_s = 2500$ m/s, $\frac{c_p c_f}{c_s^2}$ is near unity. However, exsolved gases in liquid fluid, common in shallow volcanic or geothermal environments (e.g., Kumagai & Chouet, 1999, 2001), can significantly decrease the sound speed of the mixture, resulting in a much smaller $\frac{c_p c_f}{c_s^2}$. The trade-off between C_λ and ζ in controlling $|RD/VD|$ is displayed in Figure 11. In the regime of high ζ and low C_λ, seismic radiation dominates over viscous damping, while in the regime of low ζ and high C_λ vice versa. Note that increasing λ or decreasing frequency ω while fixing other parameters increases C_λ and simultaneously decreases ζ, both of which lead to a lower percentage of damping in radiation.

6 Application to VLP seismic signals during the Mayotte volcano-seismic crisis

Since 10 May 2018, an unprecedented submarine volcano-seismic crisis occurred 30 km east of Mayotte Island (France), featuring a lithosphere-scale dyke intrusion and drainage (~ 5 km^3) of deep magma reservoirs and producing exceptionally deep seismicity and substantial surface deformation (Cesca, Letort, et al., 2020; Feuillet et al., 2021; Saurel et al., 2021; Mittal et al., 2022; Mercury et al., 2022; Retailleau et al., 2022). By mid June of 2018, sustained long duration and highly oscillatory VLP seismic signals (see an example in Figure 12a) have been observed and persist since, which are associated with resonances of magma-filled cracks excited by nearby volcano-tectonic (VT) events

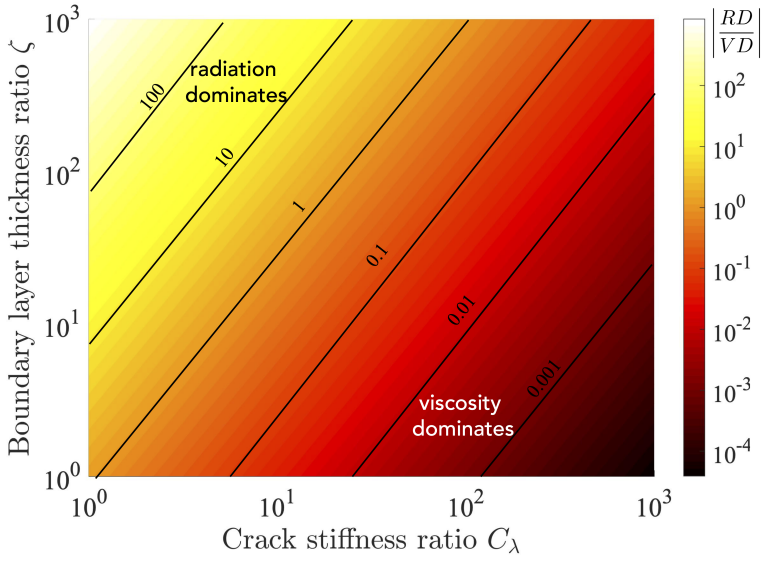

Figure 11. $|RD/VD|$ as a function of the crack stiffness ratio C_λ and the boundary layer thickness ratio ζ. Parameters used are $c_f = 1500$ m/s, $c_p = 4500$ m/s, and $c_s = 2500$ m/s.

or possible piston collapse movements (Cesca, Letort, et al., 2020; Feuillet et al., 2021). The stack of spectra of multiple VLP events reveals multiple resonant modes, among which the fundamental mode with period ∼15.5 s is present in all events, but not all higher modes are manifested in each event, probably due to differences in the excitation. The fundamental frequency can be readily explained by the crack model upon choosing a proper crack length and aperture (Cesca, Letort, et al., 2020). However, as shown in Figure 12b, the uneven spacing between resonant modes implies additional complexity in the source. Particularly, the ratio between the first higher mode and the fundamental mode is $f_2/f_1 \approx 2.5$. As shown in Figures 6 and 7, this value can not be explained by a simple rectangular or elliptical crack. Here, we show this observation can be explained by a dumbbell-shaped crack (Figure 12c). This crack shape is compatible with the f_2/f_1 data, but might still differ from the real crack geometry in Mayotte as we have not made a systematic attempt to also match the frequencies of other higher modes. However, this example is sufficient to demonstrate the potential application of the developed method. One profound question is perhaps whether one can reconstruct the topology of the crack given the information of all the resonant frequencies. Mark Kac also asked a similar question "Can one hear the shape of a drum?" (Kac, 1966). Unfortunately, the answer is negative: there exist multiple isospectral geometries that share the same resonant frequen-

cies, as mathematically proven by Gordon et al. (1992). However, these isospectral geometries are rare even though they do exist and one can still decipher the shape of the resonator given additional constraints of the vibration pattern, which in practice requires dense geophysical observation particularly in the near field. A formal inversion procedure would need to be developed in the future to find the optimal crack geometry or topology of interconnected crack networks that best explains all the observed resonant frequencies and other geophysical constraints.

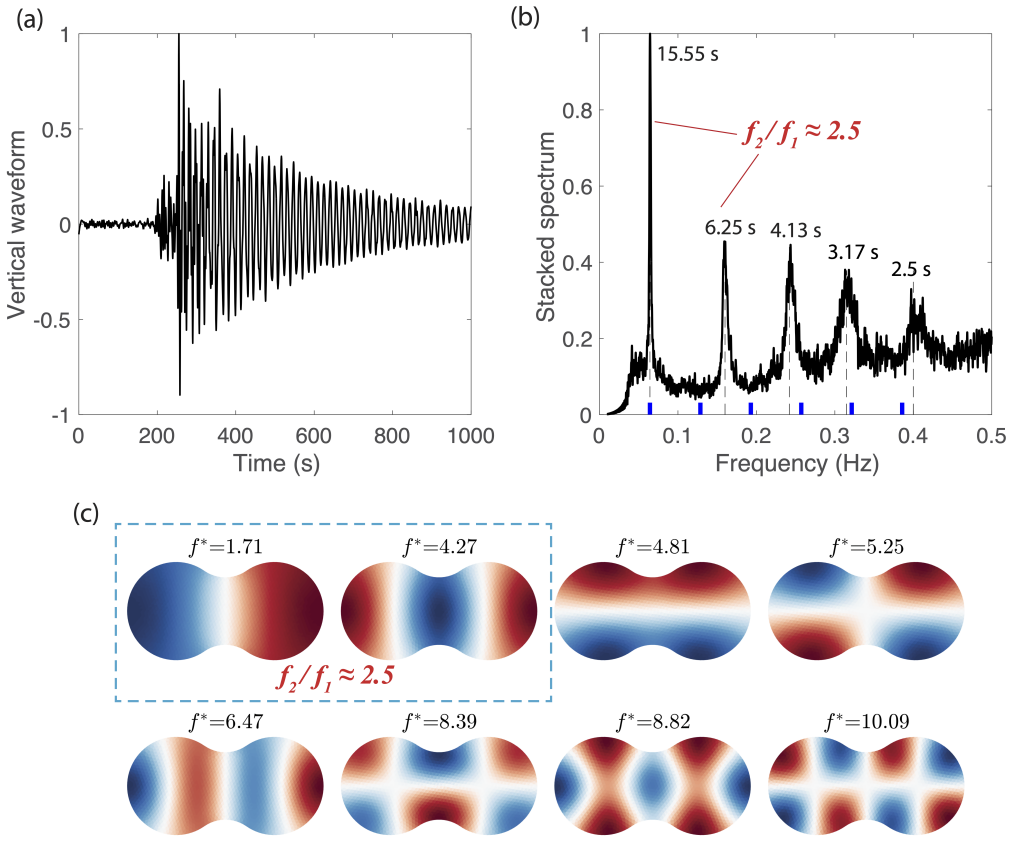

Figure 12. (a) Normalized vertical acceleration waveform of an representative VLP event (on 11 November 2018, bandpass filtered to 0.02-0.1 Hz) at the nearest broadband seismic station YTMZ on land, during the volcano-seismic crisis near Mayotte. (b) Stacked spectrum of 21 strong VLP signals compiled by Cesca, Letort, et al. (2020), highlighting multiple unevenly spaced resonant modes (dashed lines). Particularly, the frequency ratio between the first two modes $f_2/f_1 \approx 2.5$. The blue ticks indicate the integer multiples of the fundamental frequency. (c) Eigenmodes of a possible crack shape that satisfies $f_2/f_1 \approx 2.5$.

7 Summary

We have developed a hybrid method that couples the boundary element and finite volume method to efficiently compute the resonant modes of fluid-filled cracks with complex geometry. Particularly, the BEM reduces three dimensional cracks to 2D surfaces, substantially decreasing the number of degrees of freedom. By performing eigenmode analysis in the frequency domain, we avoid errors from both the time discretization and spectral analysis of the time domain data. We solve the problem in dimensionless form so that the results can be conveniently scaled to other crack sizes. After proper verification, we apply our method to an example of a crack network, revealing distinct resonant frequencies and vibration patterns, which may be utilized to infer more accurately crack shapes from seismic data.

We then systematically analyze the influence of crack aspect ratio and crack stiffness on the resonant frequencies for both rectangular and elliptical cracks, which are common models for interpreting real data. In general, rectangular and elliptical cracks share similar eigenmode types and frequencies, while the elliptical crack has slightly higher resonance frequencies due to the reduced length of the minor axis. At a high aspect ratio, the frequencies of various mode types (longitudinal, transverse and mixed) are intermingled and mode degeneration occurs. Reducing the aspect ratio increases the frequencies of all the modes, but more intensely for transverse and mixed modes than for longitudinal modes. In addition, at low aspect ratio, frequencies of modes (transverse or mixed) with the same wavelengths in the transverse direction converge and differentiating them requires additional knowledge of their vibration patterns. On the other hand, increasing C_L results in a decrease in resonant frequencies for all modes, regardless of the crack geometry, which is primarily due to the decrease in crack wave propagation speed.

The major part of this work does not consider fluid viscosity or seismic radiation, and thus cannot be used to directly compute the quality factor Q. However, by making a few assumptions, we offer additional theoretical discussion on the energy dissipation. First, by comparing numerical to analytical solutions, we confirm that the simple formula $Q = \sqrt{2}\zeta$ derived by Lipovsky and Dunham (2015) is a rather good approximation for a rectangular crack when the thickness of the viscous boundary layer is much smaller than the crack width, regardless of crack aspect ratio or vibrational mode. This is an encouraging finding that suggests one may first obtain the inviscid resonant fre-

quencies using our method and then apply analytical formula to compute Q. Note that this formula still does not consider seismic radiation. We then derived the relative ratio of the radiation damping to viscous damping, assuming a quasi-dynamic solid response on an infinite crack. We show that this ratio is primarily controlled by three dimensionless parameters: $c_p c_f / c_s^2$, C_λ and ζ. Particularly, in the limit of high ζ and low C_λ, seismic radiation dominates over viscous damping while the opposite is true in the limit of low ζ and high C_λ. Note that the seismic radiation considered here is a lower bound as we neglected the wave-mediated stresses and the seismic radiation at the finite crack tip. However, our theoretical development still offers a valuable insight into the partition of damping in crack waves.

Finally, we obtain one possible crack shape, a "dumbbell", that successfully explains the ratio of frequencies of the first two modes in the VLP seismic data during the 2018 Fani Maoré, Mayotte submarine volcanic eruption. This shape is one possibility and may be updated when additional higher modes and geophysical constraints are integrated into the analysis. In addition, the method developed here can be directly applied to other scenarios, such as unconventional oil and gas fields and glacier hydraulics. Future work requires a rigorous treatment of fluid viscosity, elastodynamics, and coupling to other geometries such as conduits and equidimensional chambers.

8 Acknowledgments

This work is funded by the early career research grant by the National Science Fundation of China (NSFC) with grant No. 42204059 and the Fundamental Research Funds for the Central Universities disseminated by IDMR at Sichuan University. It was also supported by the French government, through the UCAJEDI Investments in the Future project (ANR-15-IDEX-01) managed by the National Research Agency (ANR).

9 Data Availability Statement

The source code and the input files associated with the simulation cases are included in the Zenodo data respository at Liang et al. (2023). The VLP catalog of the Mayotte crisis is provided by Cesca, Heimann, et al. (2020) and is freely available online.

References

Aki, K., Fehler, M., & Das, S. (1977). Source mechanism of volcanic tremor: Fluid-driven crack models and their application to the 1963 Kīlauea eruption. *Journal of Volcanology and Geothermal Research*, *2*(3), 259–287. doi: 10.1016/0377-0273(77)90003-8

Aster, R. C. (2019). Interrogating a surging glacier with seismic interferometry. *Geophysical Research Letters*, *46*(14), 8162–8165. doi: 10.1029/2019GL084286

Berre, I., Doster, F., & Keilegavlen, E. (2019). Flow in fractured porous media: A review of conceptual models and discretization approaches. *Transport in Porous Media*, *130*(1), 215–236. doi: 10.1007/s11242-018-1171-6

Cao, H., Medici, E., & Askari, R. (2021). Physical modeling of fluid-filled fractures using the dynamic photoelasticity technique. *Geophysics*, *86*(1), T33–T43. doi: 10.1190/geo2020-0037.1

Cesca, S., Heimann, S., Letort, J., Razafindrakoto, H., Dahm, T., & Cotton, F. (2020). *Seismic catalogues of the 2018–2019 volcano-seismic crisis offshore mayotte, comoro islands. v. 1.0 (october 2019). available at gfz data services.* Retrieved from `https://doi.org/10.5880/GFZ.2.1.2019.004` doi: 10.5880/GFZ.2.1.2019.004

Cesca, S., Letort, J., Razafindrakoto, H. N., Heimann, S., Rivalta, E., Isken, M. P., ... others (2020). Drainage of a deep magma reservoir near mayotte inferred from seismicity and deformation. *Nature Geoscience*, *13*(1), 87–93. doi: 10.1038/s41561-019-0505-5

Chouet, B. (1986). Dynamics of a fluid-driven crack in three dimensions by the finite difference method. *Journal of Geophysical Research: Solid Earth*, *91*(B14), 13967–13992. doi: 10.1029/JB091iB14p13967

Chouet, B. A., Page, R. A., Stephens, C. D., Lahr, J. C., & Power, J. A. (1994). Precursory swarms of long-period events at redoubt volcano (1989–1990), alaska: their origin and use as a forecasting tool. *Journal of Volcanology and Geothermal Research*, *62*(1-4), 95–135. doi: 10.1016/0377-0273(94)90030-2

Cruz, F. G., & Chouet, B. A. (1997). Long-period events, the most characteristic seismicity accompanying the emplacement and extrusion of a lava dome in galeras volcano, colombia, in 1991. *Journal of Volcanology and Geothermal Research*, *77*(1-4), 121–158. doi: 10.1016/S0377-0273(96)00091-1

Durran, D. R. (2013). *Numerical methods for wave equations in geophysical fluid dynamics* (Vol. 32). Springer Science & Business Media.

Fehler, M., & Aki, K. (1978). Numerical study of diffraction of plane elastic waves by a finite crack with application to location of a magma lens. *Bulletin of the Seismological Society of America*, *68*(3), 573–598. doi: 10.1785/BSSA0680030573

Ferrazzini, V., & Aki, K. (1987). Slow waves trapped in a fluid-filled infinite crack: Implication for volcanic tremor. *Journal of Geophysical Research: Solid Earth*, *92*(B9), 9215–9223. doi: 10.1029/JB092iB09p09215

Feuillet, N., Jorry, S., Crawford, W. C., Deplus, C., Thinon, I., Jacques, E., ... others (2021). Birth of a large volcanic edifice offshore mayotte via lithosphere-scale dyke intrusion. *Nature Geoscience*, *14*(10), 787–795. doi: 10.1038/s41561-021-00809-x

Frehner, M. (2013). Krauklis wave initiation in fluid-filled fractures by a passing body wave. In *Poromechanics v: Proceedings of the fifth biot conference on poromechanics* (pp. 92–100). doi: 10.1061/9780784412992.011

Frehner, M., & Schmalholz, S. M. (2010). Finite-element simulations of stoneley guided-wave reflection and scattering at the tips of fluid-filled fractures. *Geophysics*, *75*(2), T23–T36. doi: 10.1190/1.3340361

Fujita, E., & Ida, Y. (2003). Geometrical effects and low-attenuation resonance of volcanic fluid inclusions for the source mechanism of long-period earthquakes. *Journal of Geophysical Research: Solid Earth*, *108*(B2). doi: 10.1029/2002JB001806

Geubelle, P. H., & Rice, J. R. (1995). A spectral method for three-dimensional elastodynamic fracture problems. *Journal of the Mechanics and Physics of Solids*, *43*(11), 1791–1824. doi: 10.1016/0022-5096(95)00043-I

Gordon, C., Webb, D. L., & Wolpert, S. (1992). One cannot hear the shape of a drum. *Bulletin of the American Mathematical Society*, *27*(1), 134–138. doi: 10.1090/S0273-0979-1992-00289-6

Gräff, D., Walter, F., & Lipovsky, B. P. (2019). Crack wave resonances within the basal water layer. *Annals of Glaciology*, *60*(79), 158–166. doi: 10.1017/aog.2019.8

Henry, F., Fokkema, J., & De Pater, C. (2002). Experiments on stoneley wave prop-

agation in a borehole intersected by a finite horizontal fracture. In *64th eage conference & exhibition* (pp. cp–5). doi: 10.3997/2214-4609-pdb.5.P143

Jin, Y., Zheng, Y., Huang, L., & Ehlig-Economides, C. (2022). Characterizing hydraulic fractures using the transient pressure surge effect. In *Spe/aapg/seg unconventional resources technology conference* (p. D021S028R002). doi: 10.15530/urtec-2022-3718981

Kac, M. (1966). Can one hear the shape of a drum? *The american mathematical monthly*, *73*(4P2), 1–23. doi: 10.1080/00029890.1966.11970915

Karimi-Fard, M., Durlofsky, L. J., & Aziz, K. (2004). An efficient discrete-fracture model applicable for general-purpose reservoir simulators. *SPE journal*, *9*(02), 227–236. doi: 10.2118/88812-PA

Kawakatsu, H., Kaneshima, S., Matsubayashi, H., Ohminato, T., Sudo, Y., Tsutsui, T., ... Legrand, D. (2000). Aso94: Aso seismic observation with broadband instruments. *Journal of Volcanology and Geothermal Research*, *101*(1-2), 129–154. doi: 10.1016/S0377-0273(00)00166-9

Korneev, V. (2008). Slow waves in fractures filled with viscous fluid. *Geophysics*, *73*(1), N1–N7. doi: 10.1190/1.2802174

Korneev, V., Danilovskaya, L., Nakagawa, S., & Moridis, G. (2014). Krauklis wave in a trilayer. *Geophysics*, *79*(4), L33–L39. doi: 10.1190/geo2013-0216.1

Krauklis, P. V. (1962). On some low-frequency oscillations of a fluid layer in an elastic medium. *Prikl. Mat. Mekh.*, *26*(6), 1111–1115. doi: 10.1016/0021-8928(63)90084-4

Kumagai, H., & Chouet, B. A. (1999). The complex frequencies of long-period seismic events as probes of fluid composition beneath volcanoes. *Geophysical Journal International*, *138*(2), F7–F12. doi: 10.1046/j.1365-246X.1999.00911.x

Kumagai, H., & Chouet, B. A. (2000). Acoustic properties of a crack containing magmatic or hydrothermal fluids. *Journal of Geophysical Research: Solid Earth*, *105*(B11), 25493–25512. doi: 10.1029/2000JB900273

Kumagai, H., & Chouet, B. A. (2001). The dependence of acoustic properties of a crack on the resonance mode and geometry. *Geophysical research letters*, *28*(17), 3325–3328. doi: 10.1029/2001GL013025

Kumagai, H., Miyakawa, K., Negishi, H., Inoue, H., Obara, K., & Suetsugu, D. (2003). Magmatic dike resonances inferred from very-long-period seismic

signals. *Science*, *299*(5615), 2058–2061. Retrieved from `http://science.sciencemag.org/content/299/5615/2058` doi: 10.1126/science.1081195

Li, L., & Lee, S. H. (2008). Efficient field-scale simulation of black oil in a naturally fractured reservoir through discrete fracture networks and homogenized media. *SPE Reservoir evaluation & engineering*, *11*(04), 750–758. doi: 10.2118/103901-PA

Liang, C., Karlstrom, L., & Dunham, E. M. (2020). Magma oscillations in a conduit-reservoir system, application to very long period (vlp) seismicity at basaltic volcanoes: 1. theory. *Journal of Geophysical Research: Solid Earth*, *125*(1), e2019JB017437. doi: 10.1029/2019JB017437

Liang, C., O'Reilly, O., Dunham, E. M., & Moos, D. (2017). Hydraulic fracture diagnostics from krauklis-wave resonance and tube-wave reflections. *Geophysics*, *82*(3), D171–D186. doi: 10.1190/geo2016-0480.1

Liang, C., Peng, J., Ampuero, J.-P., Shauer, N., & Dai, K. (2023, August). *Dataset for "Resonances in fluid-filled cracks of complex geometry and application to very long period (VLP) seismic signals at Mayotte submarine volcano".* Zenodo. Retrieved from `https://doi.org/10.5281/zenodo.8275079` doi: 10.5281/zenodo.8275079

Lipovsky, B. P., & Dunham, E. M. (2015). Vibrational modes of hydraulic fractures: Inference of fracture geometry from resonant frequencies and attenuation. *Journal of Geophysical Research: Solid Earth*, *120*(2), 1080–1107. doi: 10.1002/2014JB011286

Lokmer, I., Saccorotti, G., Di Lieto, B., & Bean, C. J. (2008). Temporal evolution of long-period seismicity at etna volcano, italy, and its relationships with the 2004–2005 eruption. *Earth and Planetary Science Letters*, *266*(1-2), 205–220. doi: 10.1016/j.epsl.2007.11.017

Maeda, Y., & Kumagai, H. (2013). An analytical formula for the longitudinal resonance frequencies of a fluid-filled crack. *Geophysical Research Letters*, *40*(19), 5108–5112. doi: 10.1002/grl.51002

Maeda, Y., & Kumagai, H. (2017). A generalized equation for the resonance frequencies of a fluid-filled crack. *Geophysical Journal International*, *209*(1), 192–201. doi: 10.1093/gji/ggx019

McQuillan, M., & Karlstrom, L. (2021). Fluid resonance in elastic-walled englacial

transport networks. *Journal of Glaciology*, *67*(266), 999–1012. doi: 10.1017/jog.2021.48

Mercury, N., Lemoine, A., Doubre, C., Bertil, D., van Der Woerd, J., Hoste-Colomer, R., & Battaglia, J. (2022). Onset of a submarine eruption east of mayotte, comoros archipelago: the first ten months seismicity of the seismo-volcanic sequence (2018–2019). *Comptes Rendus. Géoscience*, *354*(S2), 105–136. doi: 10.5802/crgeos.191

Métaxian, J.-P., Araujo, S., Mora, M., & Lesage, P. (2003). Seismicity related to the glacier of cotopaxi volcano, ecuador. *Geophysical Research Letters*, *30*(9). doi: 10.1029/2002GL016773

Mittal, T., Jordan, J. S., Retailleau, L., Beauducel, F., & Peltier, A. (2022). Mayotte 2018 eruption likely sourced from a magmatic mush. *Earth and Planetary Science Letters*, *590*, 117566. doi: 10.1016/j.epsl.2022.117566

Moinfar, A., Varavei, A., Sepehrnoori, K., & Johns, R. T. (2013, 07). Development of an Efficient Embedded Discrete Fracture Model for 3D Compositional Reservoir Simulation in Fractured Reservoirs. *SPE Journal*, *19*(02), 289-303. doi: 10.2118/154246-PA

Nakagawa, S., Nakashima, S., & Korneev, V. A. (2016). Laboratory measurements of guided-wave propagation within a fluid-saturated fracture. *Geophysical Prospecting*, *64*(1), 143–156. doi: 10.1111/1365-2478.12223

Nakano, M., & Kumagai, H. (2005). Response of a hydrothermal system to magmatic heat inferred from temporal variations in the complex frequencies of long-period events at kusatsu-shirane volcano, japan. *Journal of volcanology and geothermal research*, *147*(3-4), 233–244. doi: 10.1016/j.jvolgeores.2005.04.003

Nikkhoo, M., & Walter, T. R. (2015). Triangular dislocation: an analytical, artefact-free solution. *Geophysical Journal International*, *201*(2), 1119–1141. doi: 10.1093/gji/ggv035

Niu, J., & Song, T.-R. A. (2020). Real-time and in-situ assessment of conduit permeability through diverse long-period tremors beneath aso volcano, japan. *Journal of Volcanology and Geothermal Research*, *401*, 106964. doi: 10.1016/j.jvolgeores.2020.106964

Okada, Y. (1985). Surface deformation due to shear and tensile faults in a half-

space. *Bulletin of the seismological society of America*, *75*(4), 1135–1154.

Okada, Y. (1992). Internal deformation due to shear and tensile faults in a half-space. *Bulletin of the Seismological Society of America*, *82*(2), 1018–1040.

O'Reilly, O., Dunham, E. M., & Nordström, J. (2017). Simulation of wave propagation along fluid-filled cracks using high-order summation-by-parts operators and implicit-explicit time stepping. *SIAM Journal on Scientific Computing*, *39*(4), B675–B702. Retrieved from `https://doi.org/10.1137/16M1097511` doi: 10.1137/16M1097511

Paillet, F. L., & White, J. E. (1982, 08). Acoustic modes of propagation in the borehole and their relationship to rock properties. *Geophysics*, *47*(8), 1215-1228. Retrieved from `https://doi.org/10.1190/1.1441384` doi: 10.1190/1.1441384

Pointer, T., Liu, E., & Hudson, J. A. (1998). Numerical modelling of seismic waves scattered by hydrofractures: application of the indirect boundary element method. *Geophysical Journal International*, *135*(1), 289–303. doi: 10.1046/j.1365-246X.1998.00644.x

Retailleau, L., Saurel, J.-M., Laporte, M., Lavayssière, A., Ferrazzini, V., Zhu, W., ... others (2022). Automatic detection for a comprehensive view of mayotte seismicity. *Comptes Rendus. Géoscience*, *354*(S2), 153–170. doi: 10.5802/crgeos.133

Rice, J. R. (1993). Spatio-temporal complexity of slip on a fault. *Journal of Geophysical Research: Solid Earth*, *98*(B6), 9885–9907. doi: 10.1029/93JB00191

Rona, A. (2007). The acoustic resonance of rectangular and cylindrical cavities. *Journal of Algorithms & Computational Technology*, *1*(3), 329–356. doi: 10.1260/174830107782424110

Saurel, J.-M., Jacques, E., Aiken, C., Lemoine, A., Retailleau, L., Lavayssière, A., ... others (2021). Mayotte seismic crisis: building knowledge in near real-time by combining land and ocean-bottom seismometers, first results. *Geophysical Journal International*, *228*(2), 1281–1293. doi: 10.1093/gji/ggab392

Segall, P. (2010). *Earthquake and volcano deformation*. Princeton University Press. doi: 10.1515/9781400833856

Shauer, N., Desmond, K. W., Gordon, P. A., Liu, F., & Duarte, C. A. (2021). A three-dimensional generalized finite element method for the simulation of wave

propagation in fluid-filled fractures. *Computer Methods in Applied Mechanics and Engineering*, *386*, 114136. doi: 10.1016/j.cma.2021.114136

Stuart, G., Murray, T., Brisbourne, A., Styles, P., & Toon, S. (2005). Seismic emissions from a surging glacier: Bakaninbreen, svalbard. *Annals of Glaciology*, *42*, 151–157. doi: 10.3189/172756405781812538

Sun, F., Gong, Y., & Dong, C. (2020). A novel fast direct solver for 3d elastic inclusion problems with the isogeometric boundary element method. *Journal of Computational and Applied Mathematics*, *377*, 112904. doi: 10.1016/j.cam.2020.112904

Tang, X., & Cheng, C. (1988). Wave propagation in a fluid-filled fracture—an experimental study. *Geophysical Research Letters*, *15*(13), 1463–1466. doi: 10.1029/GL015i013p01463

Tang, X., & Cheng, C. (1989). A dynamic model for fluid flow in open borehole fractures. *Journal of Geophysical Research: Solid Earth*, *94*(B6), 7567–7576. doi: 10.1029/JB094iB06p07567

Tary, J.-B., Van der Baan, M., & Eaton, D. W. (2014). Interpretation of resonance frequencies recorded during hydraulic fracturing treatments. *Journal of Geophysical Research: Solid Earth*, *119*(2), 1295–1315. doi: 110.1002/2013JB010904

Xu, Y., Cavalcante Filho, J., Yu, W., & Sepehrnoori, K. (2017). Discrete-fracture modeling of complex hydraulic-fracture geometries in reservoir simulators. *SPE Reservoir Evaluation & Engineering*, *20*(02), 403–422. doi: 10.2118/183647-PA

Yamamoto, M., & Kawakatsu, H. (2008). An efficient method to compute the dynamic response of a fluid-filled crack. *Geophysical Journal International*, *174*(3), 1174–1186. doi: 10.1111/j.1365-246X.2008.03871.x

Zheng, Y., Malallah, A. H., Fehler, M. C., & Hu, H. (2016). 2d full-waveform modeling of seismic waves in layered karstic media. *Geophysics*, *81*(2), T25–T34. doi: 10.1190/geo2015-0307.1

Appendix A Matrices D and T for a simple crack intersection

In this section, we show step by step how to construct matrices **D** and **T** for a simple crack intersection shown in Figure A1. The element number and positive flux direc-

tion of each active connection as labeled. The boundary edges have zero flux and they do not contribute to **D** and **T**. Thus, we have five elements and five active connections numbered as $\{2 \to 1, 3 \to 2, 4 \to 2, 5 \to 2, 5 \to 4\}$, where $i \to j$ defines the positive flux direction. The size of both **D** and **T** are 5 by 5.

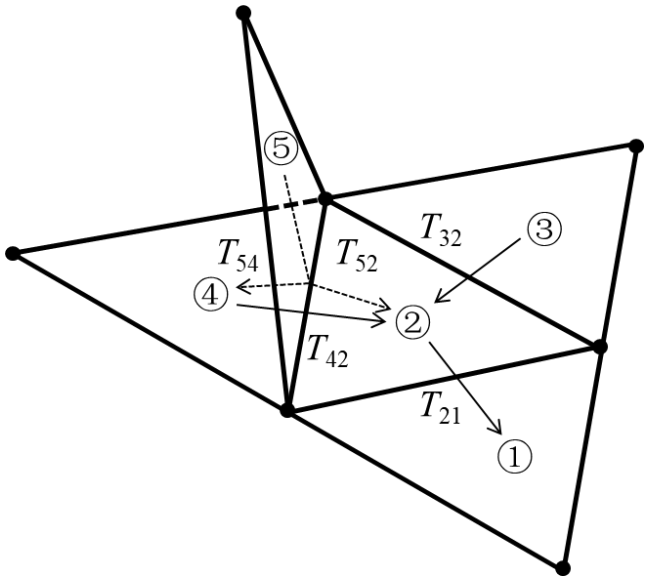

Figure A1. Geometry of a simple crack intersection. The element number and the positive flow direction of each active connection (non-zero flux) are indicated by the circled number and arrow, respectively. The scalar transmisibilities are labled near each connection.

Let's first consider the matrix **D**, which sums the flux from active connections to obtain the net out-flux from each element. We consider the first row of **D** as an example, relevant for element 1. The only connection that contributes to the net out-flux of element 1 is connection 1 with the positive direction of $2 \to 1$, the opposite to the out-flux direction. Thus, $D(1,1) = -1$ and other entries of the first row are zeros. However, for element 2, the positive flux of connection 1 aligns with the outflux direction, which leads to $D(2,1) = 1$. Similarly, other entries of matrix **D** can be determined and the matrix **D** is:

$$\mathbf{D} = \begin{bmatrix} -1 & 0 & 0 & 0 & 0 \\ 1 & -1 & -1 & -1 & 0 \\ 0 & 1 & 0 & 0 & 0 \\ 0 & 0 & 1 & 0 & -1 \\ 0 & 0 & 0 & 1 & 1 \end{bmatrix}. \tag{A1}$$

We now proceed to construct the matrix $\mathbf{T}$, which computes the flux on each active connection from the pressure on each cell. Note that we only store the flux in the positive direction. For instance, the flux on the first connection is $Q_{2\to1} = T_{21}\,(p_2 - p_1)$, which means $T(1,2) = -T(1,1) = T_{21}$. Similarly, other entries of the matrix $\mathbf{T}$ can be computed and the full expression of $\mathbf{T}$ is:

$$\mathbf{T} = \begin{bmatrix} -T_{21} & T_{21} & 0 & 0 & 0 \\ 0 & -T_{32} & T_{32} & 0 & 0 \\ 0 & -T_{42} & 0 & T_{42} & 0 \\ 0 & -T_{52} & 0 & 0 & T_{52} \\ 0 & 0 & 0 & -T_{54} & T_{54} \end{bmatrix}. \tag{A2}$$

Appendix B Resonant frequencies from time domain results by GFEM

In this section, we explain the procedure to obtain selective resonant frequencies from the time domain simulation results using the GFEM code developed by Shauer et al. (2021). As shown in Figure B1, we apply injection sources with a gaussian source time function on the certain position on the crack (red stars), obtain the pressure time series (duration of 50 s) on three receiving points (blue triangles), and then extract the resonant frequencies at spectral peaks. For the rectangular crack, we place one source at the upperleft corner, which manages to excite all the first eight modes, and three receivers (R1, R2, and R3) at (-0.5, 0), (-0.20, 0.25), and (0, 0.25), respectively. Different receivers sample different eigenmodes. For instance, receiver R1 samples modes 1, 2, 5, and 8 as shown in Figure B1-c. The modes sampled by R2 and R3 are shown in Table 2. We make this choice to selectively sample closely-spaced modes, for instance mode 2 and 3, at different receivers to avoid ambiguity.

For the elliptical crack, we place two sources at the leftmost and uppermost ends, and three receivers at (-0.5, 0), (0, 0.25), (0, 0) respectively. Due to the excitation and monitoring geometry, we focus only sampling the longitudinal and transverse modes, which are clearly seperated peaks in the spectrum. The eigenmodes sampled by different receivers are shown in Figure B1-f and Table 3.

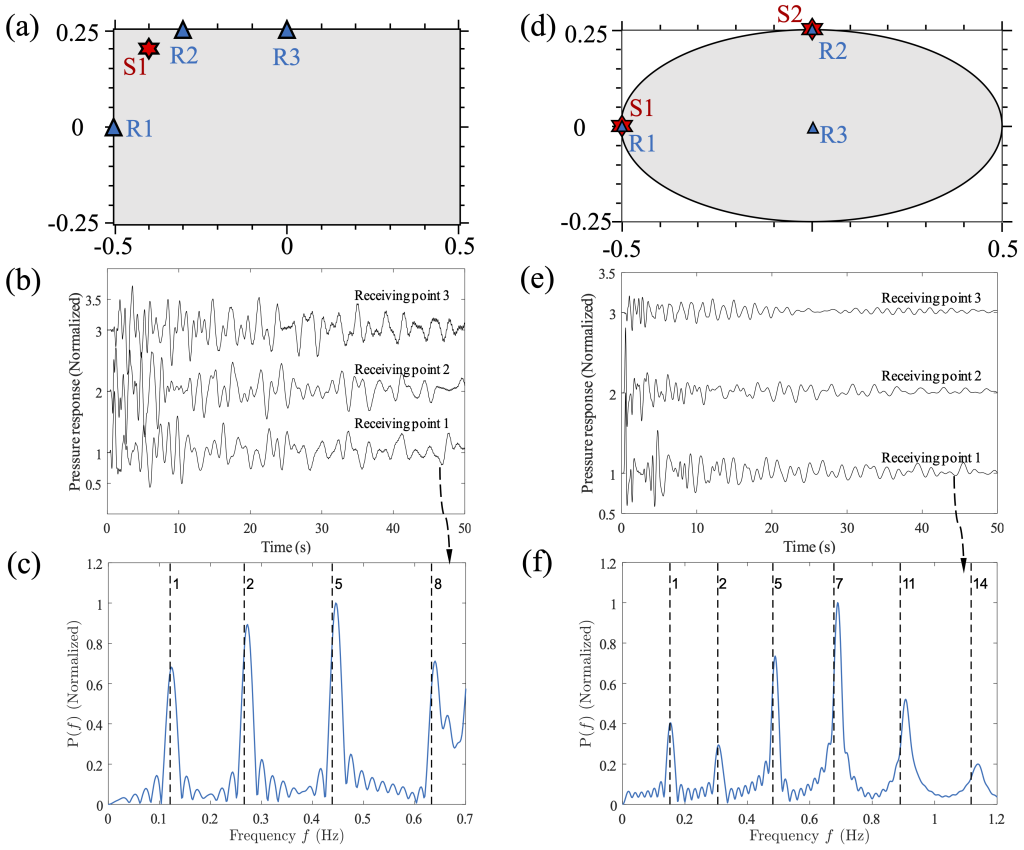

Figure B1. (a, d) The source and receiver positions. (b, e) Pressure time series at three receivers. (c, f) The normalized spectral amplitude of data at receiver R1. The vertial black dashed lines are the resonant frequencies (with mode number labelled) computed by BEM+FVM method.